MESH DEVELOPMENT OF AN INFANT FINITE ELEMENT MODEL FOR PREDICTING SKULL FRACTURE AND INTRACRANIAL HEMORRHAGE IN CHILDREN FROM LOW HEIGHT FALLS

by
Ryan Christopher Johnson

A thesis submitted to the faculty of
The University of Utah
in partial fulfillment of the requirements for the degree of

Master of Science

Department of Mechanical Engineering

The University of Utah

December 2011

The University of Utah Graduate School

STATEMENT OF THESIS APPROVAL

The thesis of **Ryan Christopher Johnson**

has been approved by the following supervisory committee members:

Brittany Coats	, Chair	**10/21/2011** Date Approved
Kenneth Monson	, Member	**10/26/2011** Date Approved
Daniel O. Adams	, Member	**10/26/2011** Date Approved

and by **Timothy Ameel**, Chair of the Department of **Mechanical Engineering**

and by Charles A. Wight, Dean of The Graduate School.

ABSTRACT

Traumatic brain injury is a leading cause of injury related deaths in the United States and children aged zero to four years are among the most likely to sustain such an injury. The most common cause is a fall; however, abuse is another common cause. Doctors are often required to determine if a child's injuries were accidental or the results of abuse. To help clinicians make the differential diagnosis a finite element model of a human infant head can be used to simulate impacts from falls and identify scenarios likely to cause skull fracture or internal hemorrhaging. Producing an accurate finite element model of an infant's head is difficult, and one of the challenges that must be overcome is the development of a stable and accurate mesh that conforms to the detailed geometry of the brain. A new meshing scheme was developed that produces geometrically accurate three-dimensional meshes of the several components present in a human head from computed tomography and magnetic resonance images. A convergence study was performed, and an appropriate mesh density that produced converged results was selected. Future work will develop an integrated finite element model of the infant head to run the simulations of low height falls for predicting head injury.

TABLE OF CONTENTS

LIST OF FIGURES

LIST OF TABLES

CHAPTER 1

INTRODUCTION

Traumatic brain injury (TBI) is a leading cause of injury-related deaths in the United States. Nationally, an estimated 1.7 million people suffer from TBI each year. Of these, about 52,000 people die, 275,000 are hospitalized, and 1.365 million visit the emergency room. Children aged 0 to 4 years are among the most likely to sustain a TBI, with the primary cause being a fall (Centers for Disease Control and Prevention 2011). Unfortunately, child abuse is another predominant cause of TBI, and caretakers suspected of abuse often initially report that the child fell. Oftentimes, the abuse is obvious and can be identified quickly. However, cases exist where the differential diagnosis between accidental and inflicted trauma is not clear, and there is a chance that a child may return to an abusive home or that the lives of innocent people may be severely disrupted by a false accusation of abuse. Therefore, the overall objective of this research is to determine the probability of injury in various fall scenarios to assist clinicians in differentiating between abusive and accidental TBI.

Biomechanics is heavily involved in the research effort to understand and reduce the incidence of TBI. In particular, finite element modeling

(FEM) is a useful tool for performing engineering stress analysis that can be used in predicting the likelihood of injury from various traumatic scenarios, such as low-height falls in infants. However, for accurate predictions, the material properties, anatomical features, and tissue-tissue interaction must be modeled appropriately.

Finite element models of the human head have commonly represented the brain and skull as simplified and idealized structures. Early adult FE studies looking at pressure changes and skull stress response modeled the skull with smooth spherical or elliptical shells and the brain as a fluid filling the spherical space (Khalil and Hubbard 1977). Later models added the brain as a solid structure and based geometry on actual head dimensions, but the brain and skull were still very simplified (DiMasi, Eppinger and Bandak 1995; Ruan, Khalil and King 1994). Current adult head FE models have become increasingly detailed and more accurate (Takhounts, et al. 2008; Watanabe, et al. 2008; Chen and Mogul 2009), but pediatric head FE models have been slow to follow.

In the 1980's, a method was developed to scale the dimension and mass of an adult FE model down to obtain a child head model (Mertz 1984). However, it has since been shown that simulations implementing this technique are likely inadequate due to changes in head shape, cranial bone thickness changes with development, and the presence of sutures and fontanels in children (Roth, Raul and Willinger 2008). Today, adult and pediatric human head geometry is commonly derived from computed tomography (CT) or magnetic resonance (MR) images. Typically, the outline of each feature is digitized and imported into software programs capable of transforming the digitized points into 3D structures. Many pediatric studies have used these images to generate 3D geometries (Coats and Margulies 2007; Roth, Raul and Willinger 2008; Willinger, Kang and Diaw 1999). However, the level of detail resulting from this method is dependent on the number of points digitized and 3D renderings may be subsequently smoothed for easier meshing.

One of the most geometrically complex components of the head is the brain. Accurate representation of the surface of the brain would include features called gyri and sulci (Figure 1). Couper and Albermani (2008) investigated the effects of incorporating brain gyri on brain stress during repetitive rotation of an infant head and concluded that the presence of gyri protrusions lessens stress in the corpus callosum and deep brain. They also concluded that the thickness specified for cerebrospinal fluid (CSF) space had a greater effect on stress predictions in the gyri model than in the model idealized as smooth. Cloots et al. (2008) also investigated the importance of including gyri and sulci, and developed numerical models to determine the influence of gyri and sulci on predictions of stress. Their results indicate that the inclusion of gyri/sulci produce higher concentrations of stress in the folds of the brain during inertial loading of the head.

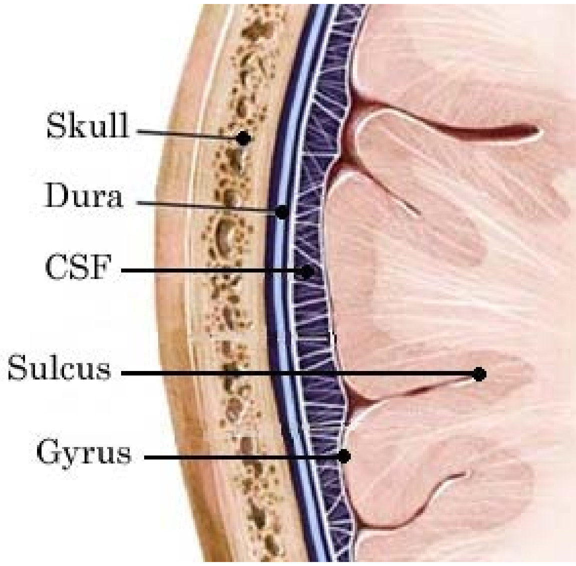

Figure 1: Section showing the various cortical structures of the brain, including gyri, sulci, and CSF.

Based on the results of these studies, it appears that the inclusion of the complex gyri and sulci geometries is most likely necessary for accurate predictions of injury near the cerebral cortex and corpus callosum.

Digitizing the gyri and sulci by hand from MR and CT images would be tedious and time consuming. One meshing method that can bypass the digitization and still achieve this level of detail is voxel-based meshing. Voxel-based meshing generates detailed 3D geometries by converting pixel data from MR or CT images into finite elements.

Briefly, MR and CT images are composed of several sequential slices through the brain (Figure 2). In each slice, pixels are assigned to anatomical objects based on pixel intensity. Each assigned pixel then registers with a similarly assigned pixel in the subsequent image, creating a 3D voxel or hexahedral shape. The completion of this process results in a 'lego-like' structure (Figure 3A). Smoothing algorithms are then employed to create a smooth, but detailed representation of the scanned object with each voxel representing the element of a mesh (Figure 3B).

This meshing technique can produce meshes containing only tetrahedral elements or a mix of tetrahedral and hexahedral elements. Tetrahedral elements can be used to model more complex geometries but FE matrices based on tetrahedrons tend to be overly stiff and may not produce accurate results. Hexahedral elements are less stiff but may result in less realistic geometry. The combination of tetrahedral and hexahedral elements plus overall mesh refinement makes smoother geometries, but this results in an extremely large number of elements and simulations become costly due to large computational times.

Because of its ability to quickly generate biofidelic geometries, voxel-based meshing was selected to generate an FE model of an infant's head for predicting probabilities of skull fracture and intracranial hemorrhage from low-height falls. The focus of this thesis is to evaluate the stability of the tetrahedral and mixed hexahedral/tetrahedral voxel-based meshing schemes, select the best meshing scheme, and begin integrating the many structures of the pediatric head into a single FE model.

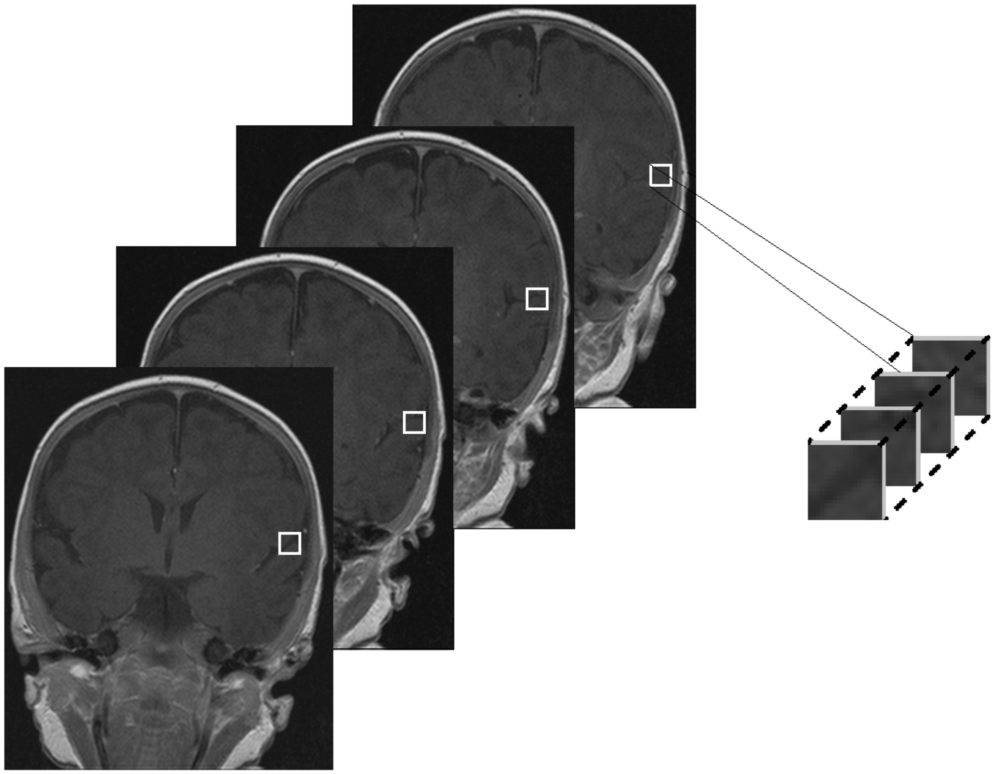

Figure 2: Some sequential MR images of the human infant head used in this study (left). Voxel based meshing takes pixels from each sequential image to create 3D voxels or hexahedral elements (right).

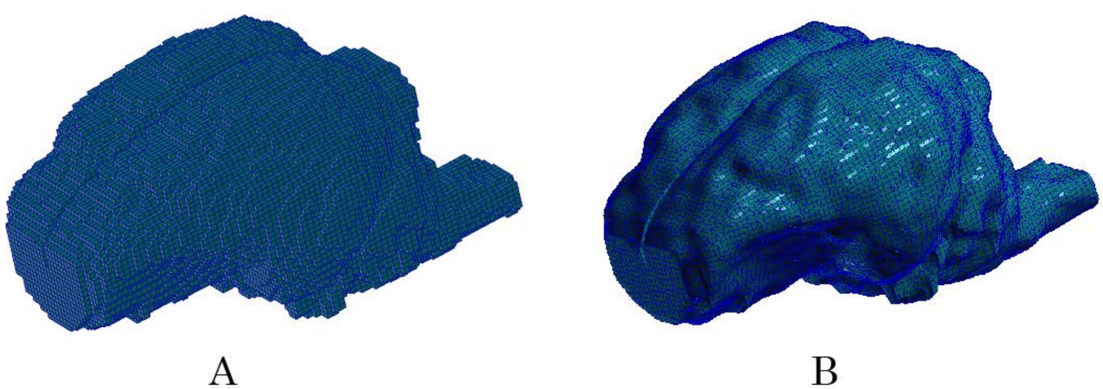

Figure 3: Example of voxel based meshing of a pig brain before (A) and after (B) smoothing algorithms are applied.

CHAPTER 2

CONVERGENCE STUDY

Model Development

Geometry.[1] Geometry for all structures in the model was obtained from MR and CT images taken of a 7 week old male experiencing fever and seizures. Upon examination, no acute brain pathology or abnormalities were found. The MR images resulted in 29 coronal slices (4 mm spacing between slices) with a 0.3125 mm in-plane resolution. The CT scan resulted in 21 horizontal slices (5 mm spacing between slices) with a 0.4882 mm in-plane resolution.

MR and CT images were imported into ScanIP (Simpleware LTD, Exeter, UK), and resampled using linear interpolation to a 1 mm cubic resolution. The CT images had a gantry tilt (angle of the CT scanner from the vertical) that was corrected by the imaging software. The images were cropped or padded to match their canvas size to each other and imported into the same model file. The CT images were aligned to the MR images using the outer skull boundary.

[1] Generation of geometry was completed previously at the University of Pennsylvania. Details are included in this thesis for clarity of the project.

All images were segmented into five cranial bones (left and right parietal, left and right frontal combined with the basal skull surface, and occipital), cranial suture, brain, and ventricles (Figure 4) by assigning pixels to objects of interest based on pixel grayscale values. Some structures were not identifiable from the images due to a lack of resolution. These include the squamosal suture and central fissure. The segmented images were refined manually to include these details based on anatomical atlases.

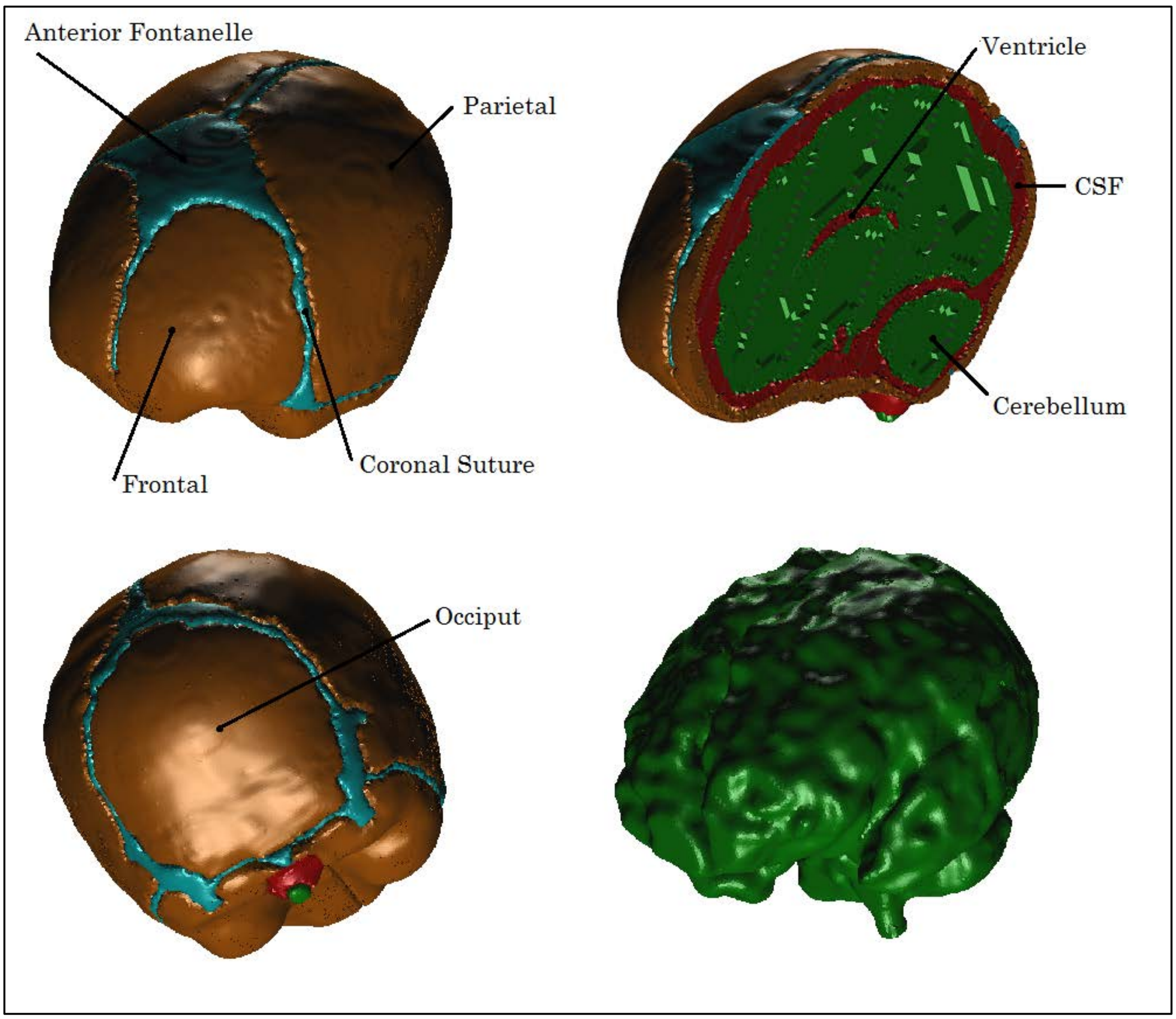

Figure 4: Infant head model showing skull (orange), suture (blue), CSF (red) and brain (green)

The CSF was also not identifiable from CT or MR images and was therefore defined as the volume inside the skull not occupied by another material. The focus of the current project is on mesh stability and development; therefore, the scalp and membranes were temporarily excluded from the model to reduce the total number of elements and save on computational time.

For each segmented region, a mask (a binary volume which describes how an object fills a space) was created, dilated 0.5-1 mm, and then smoothed using a Recursive Gaussian Filter. Dilating the masks prior to smoothing preserved the total volume of the model. Masks were evaluated in all three dimensions to ensure continuity between adjacent parts. Manual refinement was performed as necessary to eliminate holes or gaps between regions.

Material properties. The material properties for the infant brain were approximated from research done by Prange and Margulies (2002). They tested adult porcine brain tissue with stress relaxation tests in simple shear and fit data to a nonlinear constitutive model representing hyperelastic properties with the Ogden strain energy formulation (Equation 1) and viscoelastic properties with a Prony series representation (Equation 2) of the relaxation moduli. The model assumes homogeneity and isotropy of the tissue. They confirmed their model with unconfined compression experiments.

$$W = \frac{2\mu}{\alpha^2}(\lambda_1^\alpha + \lambda_2^\alpha + \lambda_3^\alpha - 3) \tag{1}$$

W is the strain energy density, α and μ are properties of the material, and λs are the principal stretch ratios.

$$\mu(t) = \mu_0 \left(1 - \sum_{i=1}^{2} C_i \left(1 - e^{-\frac{1}{\tau_i}}\right)\right) \tag{2}$$

$\mu(t)$ is the time-dependent shear modulus, C_i and τ_i are material constants.

This model was also used for the human infant head FE model, but human pediatric brain shear modulus, μ_0, was estimated by scaling published human adult values down by the ratio of measured shear modulus in adult porcine brain to that in newborn porcine brain. Material properties and constants are provided in Table 1.

The infant skull bones were modeled as orthotropic linear elastic with different elastic moduli parallel and perpendicular to the trabeculae fibers of the bone. Material properties for the skull were taken from previous studies by McPherson and Kriewall (1980), McElhaney et al. (1970), and Coats and Margulies (2006). McPherson and Kriewall (1980) used three-point bending tests to determine the elastic modulus of fetal cranial bone specimens parallel and perpendicular to trabeculae, but testing was performed at quasistatic rates. Coats and Margulies (2006) tested specimens perpendicular to trabeculae at higher rates (1.2-2.8 m/s) in infants ranging from preterm (21 weeks gestation) to one year of age, and found no significant rate-dependence compared to the quasistatic studies.

Table 1: Summary of material properties used for finite element simulations.

Material	Properties	Source
Brain	$\rho = 1.04 \times 10^3$ kg/m^3	(Prange and Margulies 2002)
	G = 601.8 Pa	Scaled from (Prange and Margulies 2002)
	$\alpha = 0.00649$	
Skull	$\rho = 2.09 \times 10^3$ kg/m^3	(McPherson and Kriewall 1980)
	$\nu = 0.19$	(McElhaney, et al. 1970)
Parietal	$E_1 = 453$ MPa	(Coats and Margulies 2006)
	$E_2 = 1810$ MPa	
	G = 662 MPa	
Occipital	$E_1 = 300$ MPa	
	$E_2 = 1200$ MPa	
	G = 503 MPa	
Suture	$\rho = 1.13 \times 10^3$ kg/m^3	(Galford and McElhaney 1970)
	$\nu = 0.49$	
	E = 8.1 MPa	(Coats and Margulies 2006)
CSF	$\rho = 1 \times 10^{-6}$ kg/m^3	(Bloomfield, Johnston and Bilston 1998)
	$\eta = 7.27 \times 10^{-4}$ Pa·s	
	K = 2.1 GPa	

The Poisson's ratio of infant cranial bone is unknown, so the Poisson's ratio, ν, of this study was assumed to be the same as adult cranial bone when compressed radially (McElhaney, et al. 1970). The shear modulus, G, was assumed to be isotropic and calculated directly with elastic modulus, E, and Poisson's ratio, ν (Equation 3).

$$G = \frac{E_2}{2(1 + \nu)} \tag{3}$$

The infant cranial suture material response was modeled as isotropic linear elastic. The elastic modulus was taken from the study done by Coats and Margulies (2006), measuring infant (<1 year old) cranial suture in tension at high rates (1.2-2.8 m/s). The Poisson's ratio and density of the suture is unknown, so it was assumed to be nearly incompressible with a density equal to dura; a membranous cranial tissue lining the inner surface of the skull (Galford and McElhaney 1970).

CSF was modeled as a Newtonian fluid (Bloomfield, Johnston and Bilston 1998) using the Mie-Gruneisen equations of state, and assuming the coefficients for the shock and particle velocity relationship are zero. This results in a directly linear relationship between pressure and volume (Equation 4), where K is the bulk modulus of CSF.

$$P = -K\frac{\Delta V}{V_0} \tag{4}$$

The shear stress (τ) of the CSF was linearly related to the strain rate ($\dot{\gamma}$) and viscosity (η) of the material (Equation 5).

$$\tau = \eta\dot{\gamma} \tag{5}$$

Boundary conditions and applied loads. A 0.8 m (2.6 ft) fall with a direct impact to the occiput of the skull was simulated. To accomplish this, the entire infant head was given an initial velocity of 4 m/s in the direction towards the fixed rigid plate. This initial velocity corresponds to the theoretical velocity of the head at impact following a 0.8 m fall. The simulations ran for 0.01 seconds, which simulated the impact of the skull to the plate and the subsequent rebounding of the head. Gravity was not included in the current study, but will be incorporated into future simulations.

The nodes of each anatomical structure were tied to those of neighboring structures. Because of complex geometries, this was best achieved by meshing all structures together and sharing surface nodes between adjacent structures. Unfortunately, the trade-off was that all structures required similar mesh densities and, therefore, regional mesh refinement was not possible; only global refinement or coarsening of the mesh was possible. A frictional interface was specified between the skull and the rigid plate with a coefficient of friction of $\mu = 0.3$.

Mesh Development

The final segmented 3D representation of the human infant head was meshed with two different meshing algorithms available in ScanIP – a tetrahedral mesh and a hybrid tetrahedral/hexahedral mesh. The tetrahedral mesh algorithm creates a mesh comprised entirely of 10-node tetrahedral elements. The hybrid mesh algorithm creates a mesh comprised of eight-node hexahedral elements and four-node tetrahedral elements. The hybrid mesh density can only be changed by resampling the images to lower or higher resolutions and remeshing. The tetrahedral mesh algorithm is able to alter mesh density by adjusting the level of adaptive surface meshing, the size of the internal elements, and how quickly the mesh transitions from small surface elements to larger internal elements. Further modification to the mesh, when needed, was performed in a separate pre-processing program (MSC Patran, Santa Ana, CA).

In the hybrid mesh, the hexahedral elements were used as much as possible for each mesh density since they are less stiff than tetrahedral elements and tend to give more accurate results (Dassault Systèmes 2010). The tetrahedral elements of the hybrid mesh were focused at anatomical surfaces and interfaces to impart a more realistic shape and contour of the human infant brain.

Convergence study. Due to the high resolution in the MR and CT images, the voxel-based meshing technique results in an extremely large number of elements and requires long processing times. Running simulations on a supercomputer cluster with multiple processors used in parallel helps to decrease computational times, but models of that size may still run for 1 to 2 days. A decrease in mesh density would greatly reduce the total number of elements in the model and significantly lower the total processing time required to run a full simulation. It was desired to find an optimal balance between feasible processing times and accuracy of results. A convergence study was performed on the skull of the infant head model with the goal of determining the coarsest mesh that could be used while still producing accurate results.

The tetrahedral mesh models were composed of slightly more than half the total number of elements of hybrid meshes using the same mesh edge length. However, the tetrahedral meshes took nearly four times as long to process as the hybrid meshes. This was caused by the fact that the mesh of ten-node tetrahedral elements resulted in nearly six times more total nodes than the mixture of four-node tetrahedral elements and eight-node hexahedral elements. Because the elements of the hybrid mesh produce more accurate results and the computational time was significantly less, the hybrid mesh was chosen to be used for the convergence analysis and all future simulations.

Two different impacts were simulated in the convergence study. The first study simulated impact to the occiput and the components included in this model were the occiput, the brain, and a rigid plate. A second study simulated impact to the right parietal bone and the components included in this model were the parietal bone, the brain, and a rigid plate. Other components of the head were not integrated into the convergence simulations to reduce variability and to save on computational time.

Each skull bone and the brain were given an initial velocity of 4 m/s towards a rigid plate to simulate a fall from 0.8 meters. The rigid plate was placed so primary impact was to the occipital bone for the first group of simulations, and to the parietal bone for the second group of simulations. A frictional interface was specified between the skull and the brain with a coefficient of $\mu = 0.3$ for the convergence study runs.

Four mesh densities of the occiput and parietal bone were created for the convergence study by changing the resolution of the images. These mesh densities, based on edge length in mm, are 1.1, 1.05, 1.0 and 0.95, (Tables 2, 3). The 1.05 mm mesh density was not used in the parietal convergence study because the mesh in the impact area was composed of mostly tetrahedral elements while the impact areas in the other meshes were composed of mostly hexahedral elements. This created geometry differences from the other mesh densities and resulted in stress that was significantly higher. For this reason, another mesh density was created (0.9 mm edge length) to take its place. One mesh of the brain was created (1.2 mm edge length) and was used across all simulations.

Simulations were processed using Abaqus/Explicit (Simulia, Providence, RI) on a supercomputer cluster available through the University of Utah's Center for High Performance Computing. Each simulation was run with 160 processors in parallel. Double precision was used for all runs.

Table 2: Number of occiput elements in each hybrid mesh density.

Mesh Density (edge length in mm)		**Percent of tetrahedral and hexahedral elements**	
Occiput Cranial Bone	Number of Elements	% Tetrahedral	% Hexahedral
Coarsest (1.1)	88,127	97.7	2.3
Coarse (1.05)	98,089	97.1	2.9
Base (1.0)	111,803	96.9	3.1
Fine (0.95)	125,118	96.5	3.5
Brain (1.2)	650,304	83.3	16.7

Table 3: Number of parietal elements in each hybrid mesh density.

Mesh Density (edge length in mm)		**Percent of tetrahedral and hexahedral elements**	
Parietal Cranial Bone	Number of Elements	% Tetrahedral	% Hexahedral
Coarsest (1.1)	151,898	97.4	2.6
Base (1.0)	195,332	97.0	3.0
Fine (0.95)	218,825	96.1	3.9
Finest (0.9)	247,798	95.8	4.2
Brain (1.2)	650,304	83.3	16.7

For reasons that remain unclear, mesh refinement of the hybrid mesh in ScanIP resulted in a slight shift in origin of the coordinate system. Therefore, to ensure all mesh densities were aligned similarly relative to the brain, preliminary simulations were started to obtain the center of mass of the skull plate and brain for each mesh density. The nodes of each mesh density were then translated using Matlab (Appendix A) until the center of mass of each skull mesh density was equal to the center of mass of the coarse (1.05 mm size) skull mesh density. Patran was then used to overlay the translated skull plates with each other to verify that they were properly aligned. Additional translations were performed, if necessary, to align the geometry of the plates as closely as possible.

Convergence analysis. Principal stress has been shown to be the best parameter to compare to the ultimate stress of cranial bone for predicting skull fracture (Coats and Margulies 2006; Coats and Margulies 2007). However, von Mises stress was selected to compare convergence simulations. The cranial bones flex during the simulations producing both tensile and compressive stresses. Von Mises stress is always positive so it was used to eliminate any errors that may have resulted from averaging positive and negative values.

The occiput was divided into nine sections (Figure 5A) and the elements of each were assigned to its corresponding section using a custom-made program in Matlab (Appendix A). Region boundaries were defined in the global coordinate system of the model and the program assigned elements to each region based on the coordinates of the first node listed for each element. Nine regions were also defined for the parietal bone (Figure 5B).

For each mesh density simulation, the von Mises stress of every skull element at every time point was extracted. The von Mises stress was then averaged across elements for each region and at each time point. The maximum average stress over time was determined using Matlab (Appendix A) and designated as the peak average von Mises stress (PAMS) for that region.

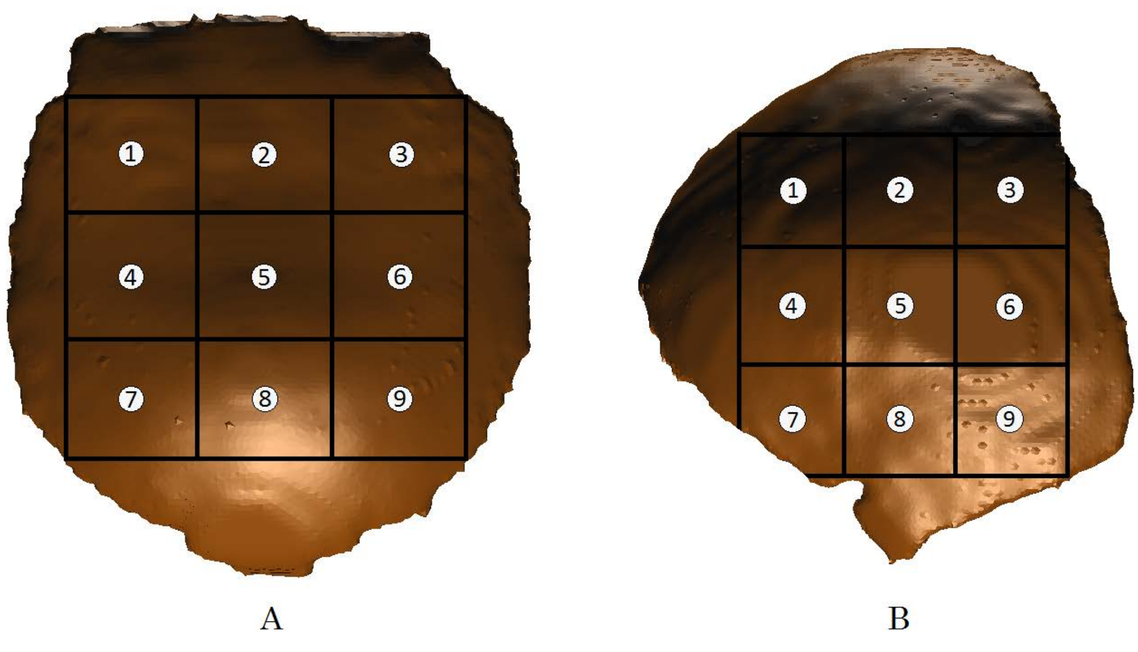

Figure 5: For each mesh density, the occiput (A) and the right parietal bone (B) were divided into nine regions. The peak average von Mises stress of each region was compared across mesh densities.

To determine convergence among the mesh densities, the PAMS for each region in each mesh density was subtracted from the PAMS of the corresponding region of the densest mesh. The differences were squared and summed across regions to calculate the residual sum of squares (RSS) for each mesh density (Equation 6).

$$RSS = \sum_{n=1}^{9} \left(\sigma_c - \sigma_f\right)^2 \tag{6}$$

where σ_c is the PAMS of the mesh being evaluated and σ_f is the PAMS of the finest mesh. The RSS is a measure of the discrepancy or variance between each mesh density with the finest mesh.

The PAMS of each region of the <u>finest</u> mesh were summed and divided by the total number of regions (n = 9). This average value ($\bar{\sigma}_f$) was subtracted from each regional PAMS and squared. These squared differences were summed to calculate the total sum of squares (TSS) (Equation 7).

$$TSS = \sum_{n=1}^{9} (\sigma_f - \bar{\sigma}_f)^2 \tag{7}$$

The TSS is a measure of the overall variability of the results of the finest mesh.

To determine convergence, the ratio of RSS to TSS, which normalizes the total variation between the mesh densities, was calculated and plotted versus the number of elements of each mesh density. This ratio is termed the coefficient of nondetermination and is an indication of the normalized relative differences between each coarser mesh and the finest mesh. Values close to zero indicate that the mesh results are very similar, and ratios near a value of one would indicate that observed differences between mesh densities are similar to the natural variation of the finest mesh and are acceptable values. Values above one are indicative of differing results between mesh densities that fall outside the range of variation with the finest mesh, which would imply that the results are not converged (Zar 2010).

CHAPTER 3

RESULTS

The RSS/TSS ratios from the occiput convergence results were tabulated (Table 4) and plotted versus the total number of elements in the occiput (Figure 6).

The ratios from the occiput simulations are all less than 0.2 which indicates that the differences between mesh densities are well within the acceptable range of zero to one, and are converged. As an additional validation of convergence, the average percent difference of the PAMS results across all regions was calculated for each mesh density versus the finest mesh. The coarsest mesh (1.1 mm) had an average percent difference of 11% and the 1.05 mm and 1.0 mm meshes had percent differences of 2.3% and 3.2%, respectively.

The 0.046 RSS/TSS ratio of the 1.0 mm size mesh indicates that its results are well converged. It is also the coarsest size which fully captures all anatomical details of the sutures. Coarser meshes derived from lower resolution CT and MR images resulted in holes in the thinnest regions of the sutures. Therefore, 1.0 mm was the mesh density chosen to be used for simulations integrating all the components of the head.

Table 4: RSS/TSS ratios for the four mesh densities and the number of occiput elements.

Occiput Mesh Density (edge length in mm)	# Elements	RSS/TSS
Coarsest (1.1)	88,127	0.193
Coarse (1.05)	98,089	0.114
Base (1.0)	111,803	0.0464
Fine (0.95)	125,118	0

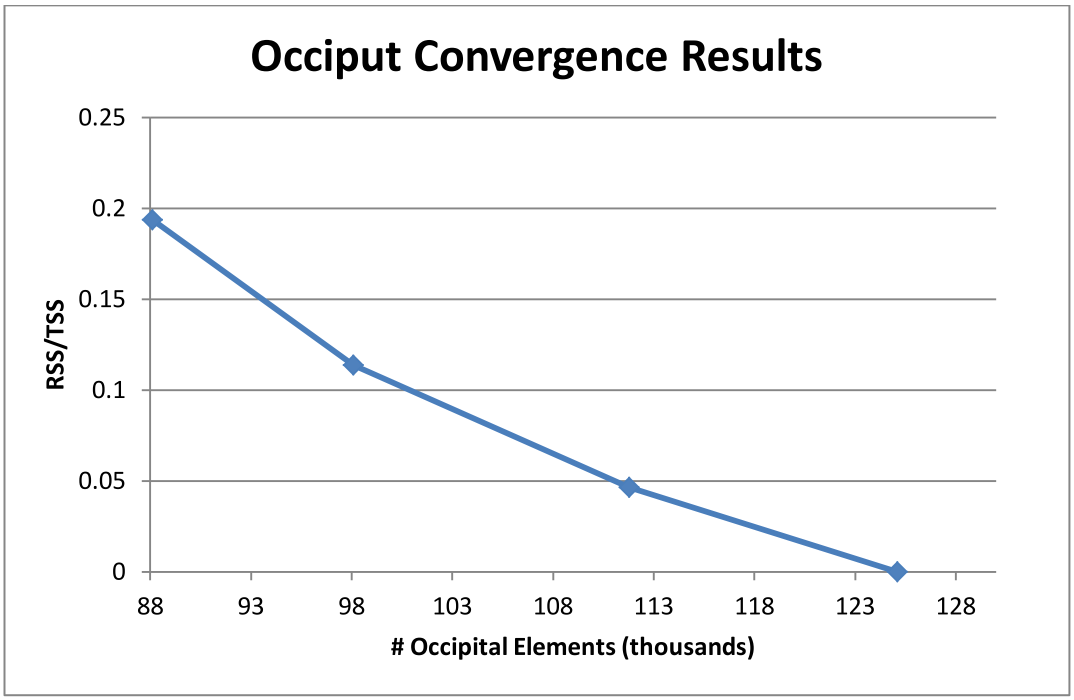

Figure 6: RSS/TSS ratios versus number of occipital elements.

The RSS/TSS ratios from the parietal convergence results were tabulated (Table 5) and plotted versus the total number of elements in the parietal bone (Figure 7). The plot has some oscillation, however, the highest RSS/TSS ratio value of 0.69 for the 1.0 mm size mesh is still less than one which indicates that the results are within the range of the natural variation of the finest mesh and are acceptably converged. This is further supported by the small percent differences between the parietal PAMS of each coarser mesh density and the finest mesh. The 1.1 mm, 1.0 mm, and 0.95 mm meshes had average percent differences of 7.3%, 12.1%, and 3.2%, respectively.

Table 5: RSS/TSS ratios for the four mesh densities and the number of parietal bone elements.

Parietal Mesh Density (edge length in mm)	# Elements	RSS/TSS
Coarsest (1.1)	151,898	0.484708
Base (1.0)	195,332	0.689601
Fine (0.95)	218,825	0.072053
Finest (0.9)	247,798	0

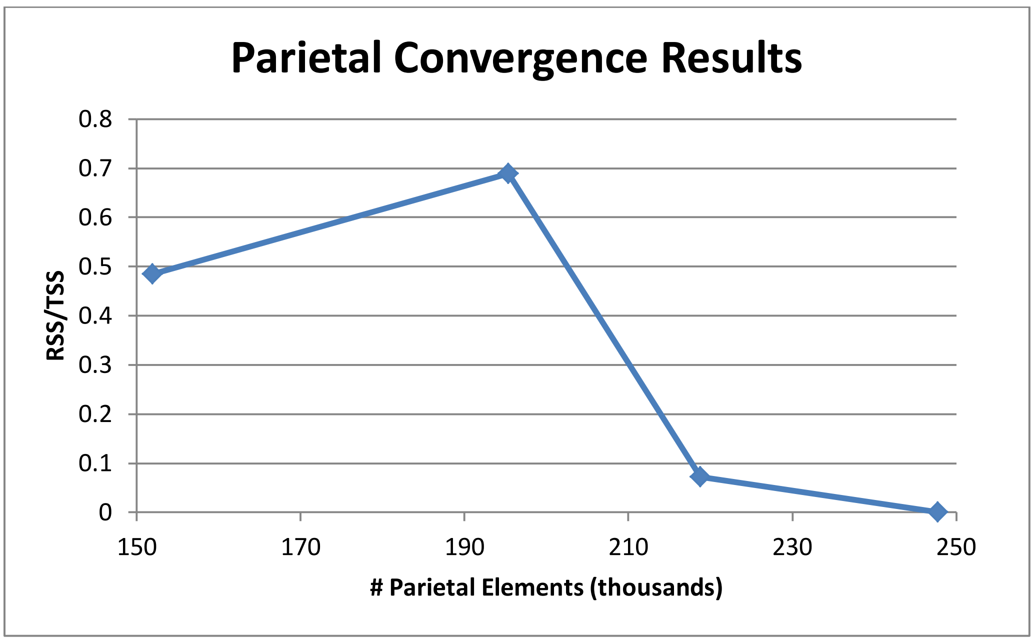

Figure 7: RSS/TSS ratios versus number of parietal elements.

CHAPTER 4

DISCUSSION

All of the meshes created in this study are high density meshes, so it was expected that results would be converged across mesh densities and there would be little difference between regional PAMS. The plot of the results for the occiput convergence study does not exhibit a plateau region that is typical of most convergence studies. This is because all of the meshes investigated are of an extremely high density and the plots are likely focused on the differences within the plateau region. This is supported by the small changes in the RSS/TSS ratios and percent differences, indicating that the results are adequately converged. The plot of the results for the parietal convergence study oscillates but the RSS/TSS ratios are still below one which means they fall within the range of the natural variance of the finest mesh. However, the parietal convergence study results helped reveal some sources of error that affected convergence results.

The first source of error was from slight changes in the shape of the skull with different mesh densities. This occurred because mesh refinement or coarsening of the hybrid mesh was created by resampling CT and MR images at different resolutions. The resampling varied the pixels assigned to each component, resulting in small geometrical changes. These geometry changes altered the stress distribution in the elements, especially if they were located in the region of impact. To minimize this error, resampling parameters were selected to reduce geometric changes in the region of impact. This eliminated most of the variation, but there were still some geometric differences between mesh densities, particularly along the edges of components. This was most evident in the parietal bone (1.0 mm mesh), which had visible geometric differences near the area of impact and resulted in slightly larger RSS/TSS ratios. In addition, the 1.05 mm edge length mesh was not used in the parietal study because it was too dissimilar from the other meshes to be able to compare the results. The area of impact in the 1.05 mm mesh was comprised of tetrahedral elements. On the other hand, the area of impact in every other mesh density was comprised mostly of hexahedral elements. The resulting stresses in the stiffer tetrahedral elements of the 1.05 mm mesh were significantly higher. For this reason, it was decided to not use the 1.05 mm mesh in the parietal convergence study. Instead, a new finer mesh with a 0.9 mm edge size was created. This mesh had an area of impact similar to the other meshes which was comprised mostly of hexahedral elements and the results it produced were very similar to the other meshes' results. This error should not be great enough in the 1.0 mm size mesh to impair the future validation of the model to predict injury.

Another source of error stems from how the nine regions of the occiput and parietal bone were defined. Initially, a grid was placed over the occiput and each region was manually selected so that the von Mises stress could be extracted from the selected elements. Using this method, elements lying on region borders were frequently selected twice as a part of both of the adjacent regions and it was difficult to consistently select the same region areas across all mesh densities. Variability was also present due to the fact that the skulls from different mesh densities were not aligned perfectly with each other.

To minimize error due to region definition, global coordinates along the primary axes in the model were used to define the boundaries of each region. A custom Matlab program (Appendix A) looked at the coordinates of the first node listed for each element and assigned elements to their corresponding regions based on those coordinates. This method ensured that elements did not belong to more than one region and the defined grid boundaries were always the same. There may still be some variability due to imperfect alignment of the skulls with each other, resulting in region boundaries shifting slightly from one mesh density to the next.

One final possible source of error was the varying ratio of tetrahedral to hexahedral elements present in each mesh. If one mesh contained a higher ratio of tetrahedral to hexahedral elements than another mesh then its resulting stress concentrations could be higher because tetrahedral elements tend to be stiffer than hexahedral elements. This was most apparent in the results of the 1.05 mm mesh of the parietal bone which was removed from the convergence study. The percentage of tetrahedral and hexahedral elements in each mesh density does appear to correlate with RSS/TSS ratios, with higher percentages of tetrahedral elements roughly corresponding to higher RSS/TSS ratios. However, it is difficult to determine whether this error is caused by the accuracy of the elements themselves or is due to differences in the geometry.

CHAPTER 5

MODEL COMPONENT INTEGRATION

Model Description

The infant head model will be composed of five cranial bones, cranial sutures, brain, ventricles, CSF, membranes, scalp, falx, and tentorium. To test the interaction of these components, a fall from 2.6 feet with primary impact to the occiput was simulated. Initial simulations of all components together resulted in failures mostly due to initial overlapping of elements of different components. Therefore, the objective of this study was to create an FE model that integrates all of the components meshed with the voxel-based meshing technique. Because the goal was to successfully complete a simulation of all components together with their interactions, accuracy of the results was not assessed and will be the topic of a future study.

To identify and resolve interaction problems, simulations were performed first with the skull alone and then components were added one at a time, fixing errors along the way, until a simulation of the whole model ran to completion.

Skull and Sutures

The first simulation of the five cranial bones of the skull completed successfully. A mesh of the sutures was then added to the skull. The mesh of the sutures was created separately from the skull mesh so they were tied together using a tie tolerance of 0.1 mm. Unfortunately, the combination of the two different meshes contained many overclosures between the suture and skull elements. These overclosures caused the simulations to fail quickly, sometimes even before the rigid plate collided with the occiput. To eliminate overclosures, the skull and suture were remeshed together so nodes were shared at the interface of the two components.

This new mesh had an edge length of 1.0 mm and was selected because it was the coarsest density that could capture all the suture geometry. Coarser mesh densities derived from lower resolutions of the resampled CT and MR images resulted in voids or holes in regions of the suture because the minimum thickness of the suture was approximately 1 mm. Shared nodes were effectively tied together, so the tie tolerance specification was deleted. The new mesh eliminated overclosures and the simulation completed successfully.

Skull, Sutures, and Brain

Next, the brain was added to the skull and sutures. Because the brain has a solid geometry, a coarser mesh (1.2 mm size) was used with the 1.0 mm skull and suture mesh. No overclosures were present because CSF lies between the skull and brain, and it was not yet incorporated into the model, leaving ample space between the brain and skull. The first simulation with all three components failed due to excessive deformation of the brain elements that came into contact with the occiput. With the additional components of CSF, ventricles, falx, and tentorium, it is estimated that the deformation of the brain would not be as large. Therefore, the shear modulus of the brain was temporarily increased by a factor of 10. Once all components are successfully integrated, the stiffness will be returned to its original value. The simulation with the increased modulus completed successfully.

Skull, Sutures, Brain, and CSF

The next component added to the model was the CSF with a mesh edge length of 1.0 mm. The CSF nodes were tied to the skull and brain surfaces using a tie tolerance of 0.1 mm. This tolerance did not result in all of the CSF surface nodes tying to adjacent components, especially around the sulci, and resulted in premature failure of the FE model. Adjustments to the tie tolerance resulted in too few or too many nodes tied, so alternative methods were explored.

Creating a list of the surface nodes to be tied manually was investigated, but because of the number of nodes and dense configuration, distinguishing internal nodes, surface nodes next to the brain, and surface nodes next to the skull proved difficult. Instead, it was decided that the most efficient way to tie components together without including overclosures was to produce a mesh of all components at the same time so that component interfaces shared nodes. Thus, the brain, skull, suture, and CSF were remeshed together with an edge length of 1.0 mm. Despite meshing all components together, gaps were still found between the CSF and the skull or sutures. To fix this problem, the node numbers belonging to the surface elements around the untied regions were identified and manually tied. This new mesh was successful in eliminating initial overclosures and tying the entire CSF surface to the brain and skull, but computational time was increased.

Even with well-defined contact among the CSF, brain, skull, and sutures, CSF elements commonly failed due to excessive deformation. Failed elements were always located on the interface with the skull and suture, and were likely due to the low deviatoric properties used in the constitutive model of CSF. This resulted in large displacements of the internal CSF nodes while surface CSF node displacements were dominated by the stiffer brain and skull material properties. This was most visible at the foramen magnum – the large hole at the base of the skull through which the spinal cord passes. Following impact of the occiput to the plate, the brainstem and CSF moved out of the foramen magnum (Figure 8). However, because the CSF is tied to the skull (i.e. the foramen magnum), the internal nodes displaced out of the skull while the surface nodes remain fixed, creating excessive deformation of the CSF elements (Figure 9).

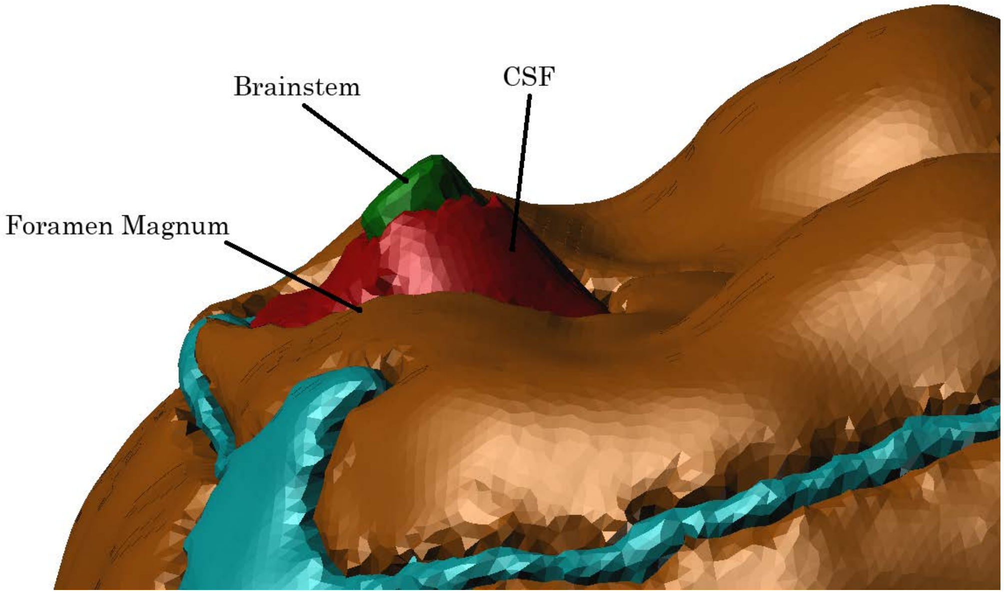

Figure 8: Image of the base of the skull showing the brainstem and CSF protruding out of the foramen magnum.

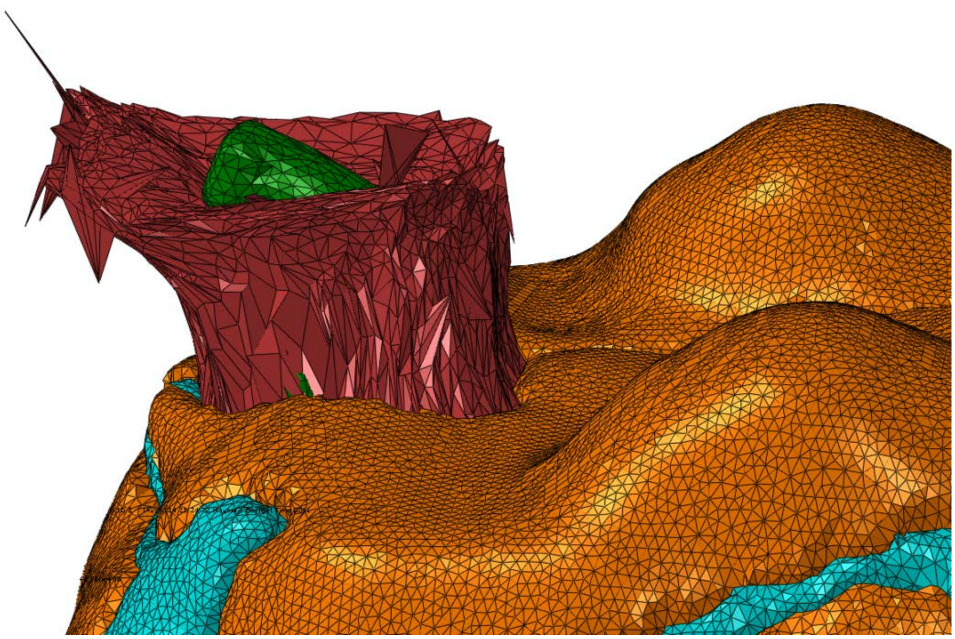

Figure 9: Image from simulation showing large deformation in CSF because external nodes are tied to skull, but internal nodes move freely out of the foramen magnum.

To fix this problem, future studies should focus on alternative interactions between the CSF and the brain and skull. CSF is a Newtonian fluid that flows freely relative to the brain and skull. More appropriate contact algorithms should allow tangential slip. Another alternative is to incorporate the CSF as an Eulerian material. This would allow CSF to flow independently of the mesh.

Brain, Skull, Suture, and Membranes

Current work in the lab is being done to integrate the membranes with the brain, skull, and suture while strategies to incorporate CSF are being explored. Successful incorporation of membranes and CSF will be followed by the inclusion of the scalp. Once complete, the stiffness of the brain will be lowered to its original modulus value and work will continue toward evaluation of the accuracy of the human infant FE model.

CHAPTER 6

CONCLUSIONS

Convergence Study

The convergence study confirmed that the meshes generated in this study are high density meshes which produce converged results. The hybrid mesh is a more desirable mesh than the tetrahedral mesh because its simulations process approximately four times faster and the inclusion of hexahedral elements should produce more accurate results. The inclusion of the tetrahedral elements on the surfaces permitted the meshes to have truer and smoother geometries.

Even though the generated meshes were well refined, some geometrical differences were visible between different mesh densities. The edges around the cranial bones were the most obvious areas where disparities in the contours existed. Despite these minor geometrical variations in the meshes used for the convergence study, the low RSS/TSS ratios indicate that any error due to these differences was minimal. On the other hand, the 1.05 mm mesh that was removed from the parietal convergence study may have produced its significantly higher results due to these geometrical differences. The future validation of this model with the

1.0 mm mesh may have to address this issue if stresses are too high in the model. A possible fix to this issue would be to take more CT or MR images with smaller spacing between slices so that less interpolation is required, thus rendering a truer overall geometry.

Component Integration

The voxel-based meshing scheme is an efficient way to quickly reproduce the complex three-dimensional geometries of a human head. However, integration of separately created meshes with complex geometries will result in the inclusion of overclosures which always cause simulations to fail. Meshing all components together is the only feasible way to prevent inclusion of overclosures in these high density meshes but this method also automatically ties components together along their interfaces of shared nodes. This may or may not be desirable in the FE model. If it is not desired to tie components together, the nodes could be separated by writing a program which renumbers only the nodes of the component to be detached. This would create a new set of nodes with the same coordinates as before but without being tied to the shared interface. Another downside of meshing together is that computational time cannot be decreased by including coarser densities for some components.

In conclusion, there are many trade-offs with the voxel based meshing technique, and the appropriateness of its use in FE models depends greatly on the size and scope of the model and the desired interactions at component interfaces. Many of the limitations of using the meshing scheme for the human infant FE model may be overcome, and having a detailed geometry is likely important in predictions of head injury, so it is recommended that investigation using this meshing scheme continue for the human infant FE model.

APPENDIX A

CUSTOM-MADE MATLAB CODES

Matlab Code to Translate Node Values

Note: Must import the node file created by Patran manually. This original node file will be named “data.”

```
% Node_Translator

% This file translates nodes

Nodes_1p0 = zeros(length(data),4);

% Translation values
x = 1;
y = 1;
z = 1;

% Translate the original node file to new values
Nodes_1p0(:,1) = data(:,1);
Nodes_1p0(:,2) = data(:,2) + x;
Nodes_1p0(:,3) = data(:,3) + y;
Nodes_1p0(:,4) = data(:,4) + z;

% Command to write new node values file
% dlmwrite('filename.inp', Nodes_1p0, 'precision', '%.4f')
```

Matlab Code to Create Input for 'Element_sort_all' Code

Note: The element file created by Patran must be used to create separate files of the hexahedral elements and the tetrahedral elements which are manually imported into Matlab before this code is run. The elm1 and elm2 outputs from this code are saved along with the translated nodes file to create the input needed for the Element_sort_all code.

```
% Elm_Creator

% Create elm1 and elm2 for Element_sort_all code

elm1 = zeros(length(x1p0_tetelms),2);
for i=1:length(x1p0_tetelms)
    elm1(i,1) = x1p0_tetelms(i,1);
    elm1(i,2) = x1p0_tetelms(i,2);
end

elm2 = zeros(length(x1p0_hexelms)/2,2);
for j=1:length(x1p0_hexelms)/2
    elm2(j,1) = x1p0_hexelms(2*j-1,1);
    elm2(j,2) = x1p0_hexelms(2*j-1,2);
end
```

Matlab Code ‘Element_sort_all’ Which Assigns Elements to Each Region

Note: This code outputs nine regions which must all be saved together in a file to be used as an input to the Data_extract code (A.4).

%Element_sort_all

```
%% Separates elements into regions based on coordinates of the first
% node in each element.

clc
clear

%% Load element node data set
% There are 3 inputs in each file:
%   1) nodes - list of all nodes in the model with the associated
% coordinates
%   2) elm1 - list of the tet elements in the occiput with the first
% node listed in its node list
%   3) elm2 - list of the hex elements in the occiput with the first
% node listed in its node list

% Change which file is loaded for each mesh
load x1p1_nodelm
% load x1p05_nodelm
% load x1p0_nodelm
% load p95_nodelm
% load p90_nodelm


%% Transform nodes in z-y plane by rotating about the x-axis
R=[cosd(-45) -sind(-45);sind(-45) cosd(-45)];


%% Select cutoffs for regions
%Note: Only y and z components are transformed about the x-axis.

comcoarse=[66.55669 (R*[77.13514 77.63508]')'];
combase=[66.55674 (R*[77.13519 77.63509]')'];
comlilfiner=[66.55668 (R*[77.13513 77.6351]')'];
comfinest=[66.55669 (R*[77.13511 77.63509]')'];

%coarse
delta=comcoarse-comcoarse;

%base
% delta=comcoarse-combase;

%lilfiner
% delta=comcoarse-comlilfiner;
```

```
%finest
% delta=comcoarse-comfinest;

ax=43.5-delta(1);bx=61-delta(1);cx=78.5-delta(1);dx=95.4-delta(1);
ay=-18.2-delta(3);by=-1.4-delta(3);cy=15-delta(3);dy=31-delta(3);

%% Sort elements based on first node location (9 regions)
a=1;b=1;c=1;d=1;e=1;f=1;g=1;h=1;j=1;
for i=1:length(elm1)
    z=find(elm1(i,2)==nodes(:,1));
    nodesm=[nodes(z,1:2) (R*nodes(z,3:4)')'];
    if isempty(z)==1
        break
        z
    elseif nodesm(2)>=ax&&nodesm(2)<bx
        if nodesm(4)>=ay&&nodesm(4)<by
            Region1(a)=elm1(i,1);
            a=a+1;
        elseif nodesm(4)>=by&&nodesm(4)<cy
            Region4(b)=elm1(i,1);
            b=b+1;
        elseif nodesm(4)>=cy&&nodesm(4)<dy
            Region7(c)=elm1(i,1);
            c=c+1;
        end
    elseif nodesm(2)>=bx&&nodesm(2)<cx
        if nodesm(4)>=ay&&nodesm(4)<by
            Region2(d)=elm1(i,1);
            d=d+1;
        elseif nodesm(4)>=by&&nodesm(4)<cy
            Region5(e)=elm1(i,1);
            e=e+1;
        elseif nodesm(4)>=cy&&nodesm(4)<dy
            Region8(f)=elm1(i,1);
            f=f+1;
        end
    elseif nodesm(2)>=cx&&nodesm(2)<dx
        if nodesm(4)>=ay&&nodesm(4)<by
            Region3(g)=elm1(i,1);
            g=g+1;
        elseif nodesm(4)>=by&&nodesm(4)<cy
            Region6(h)=elm1(i,1);
            h=h+1;
        elseif nodesm(4)>=cy&&nodesm(4)<dy
            Region9(j)=elm1(i,1);
            j=j+1;
        end
    end
end

for i=1:length(elm2)
    z=find(elm2(i,2)==nodes(:,1));
    nodesm=[nodes(z,1:2) (R*nodes(z,3:4)')'];
    if isempty(z)==1
        break
```

```
        z
    elseif nodesm(2)>=ax&&nodesm(2)<bx
        if nodesm(4)>=ay&&nodesm(4)<by
            Region1(a)=elm2(i,1);
            a=a+1;
        elseif nodesm(4)>=by&&nodesm(4)<cy
            Region4(b)=elm2(i,1);
            b=b+1;
        elseif nodesm(4)>=cy&&nodesm(4)<dy
            Region7(c)=elm2(i,1);
            c=c+1;
        end
    elseif nodesm(2)>=bx&&nodesm(2)<cx
        if nodesm(4)>=ay&&nodesm(4)<by
            Region2(d)=elm2(i,1);
            d=d+1;
        elseif nodesm(4)>=by&&nodesm(4)<cy
            Region5(e)=elm2(i,1);
            e=e+1;
        elseif nodesm(4)>=cy&&nodesm(4)<dy
            Region8(f)=elm2(i,1);
            f=f+1;
        end
    elseif nodesm(2)>=cx&&nodesm(2)<dx
        if nodesm(4)>=ay&&nodesm(4)<by
            Region3(g)=elm2(i,1);
            g=g+1;
        elseif nodesm(4)>=by&&nodesm(4)<cy
            Region6(h)=elm2(i,1);
            h=h+1;
        elseif nodesm(4)>=cy&&nodesm(4)<dy
            Region9(j)=elm2(i,1);
            j=j+1;
        end
    end
end
```

Matlab Code 'Data_extract' Which Calculates the Peak Average Von Mises Stress for Each Region

Note: Inputs for this file include the nine regions file created by the Element_sort_all code as well as the 20 von Mises stress data files which were created in Abaqus CAE. The output of this code, peakVM, is the peak average von Mises stress which was used to calculate the RSS/TSS ratios for the convergence study.

%Data_extract

```
clc
clear all

%% load the entire occiput data
% This will import each of your von mises time step files from CAE.
% There are 20 files in all.

% Change to the desired mesh density
for i=1:20
importfile(['Coarsest_occiput_mises_step' num2str(i) '.rpt'])
% importfile(['Coarse_occiput_mises_step' num2str(i) '.rpt'])
% importfile(['Base_occiput_mises_step' num2str(i) '.rpt'])
% importfile(['LilFiner_occiput_mises_step' num2str(i) '.rpt'])
% importfile(['Finest_occiput_mises_step' num2str(i) '.rpt'])
VM(:,i)=data(:,2);
end

labels=data(:,1);
VM=[labels VM];

%% load region definitions
%This loads your region definition files
%Change code here for each mesh density

load x1p1_regions
% load x1p05_regions
% load x1p0_regions
% load p95_regions
% load p90_regions

peakVM=[];
%% Region 1
j=1;
for i=1:length(Region1)
    index=find(Region1(i)==VM(:,1));
    if isempty(index)~=1
        VM1(j,:)=VM(index,:);
        j=j+1;
    end
end
```

```
for k=2:21
    aveVM1(k-1)=mean(VM1(:,k));
end
maxVM1=max(aveVM1);
peakVM=[peakVM; maxVM1];

%% Region 2
j=1;
for i=1:length(Region2)
    index=find(Region2(i)==VM(:,1));
    if isempty(index)~=1
        VM2(j,:)=VM(index,:);
        j=j+1;
    end
end

for k=2:21
    aveVM2(k-1)=mean(VM2(:,k));
end
maxVM2=max(aveVM2);
peakVM=[peakVM; maxVM2];

%% Region 3
j=1;
for i=1:length(Region3)
    index=find(Region3(i)==VM(:,1));
    if isempty(index)~=1
        VM3(j,:)=VM(index,:);
        j=j+1;
    end
end

for k=2:21
    aveVM3(k-1)=mean(VM3(:,k));
end
maxVM3=max(aveVM3);
peakVM=[peakVM; maxVM3];

%% Region 4
j=1;
for i=1:length(Region4)
    index=find(Region4(i)==VM(:,1));
    if isempty(index)~=1
        VM4(j,:)=VM(index,:);
        j=j+1;
    end
end

for k=2:21
    aveVM4(k-1)=mean(VM4(:,k));
end
maxVM4=max(aveVM4);
peakVM=[peakVM; maxVM4];
```

```
%% Region 5
j=1;
for i=1:length(Region5)
    index=find(Region5(i)==VM(:,1));
    if isempty(index)~=1
        VM5(j,:)=VM(index,:);
        j=j+1;
    end
end

for k=2:21
    aveVM5(k-1)=mean(VM5(:,k));
end
maxVM5=max(aveVM5);
peakVM=[peakVM; maxVM5];

%% Region 6
j=1;
for i=1:length(Region6)
    index=find(Region6(i)==VM(:,1));
    if isempty(index)~=1
        VM6(j,:)=VM(index,:);
        j=j+1;
    end
end

for k=2:21
    aveVM6(k-1)=mean(VM6(:,k));
end
maxVM6=max(aveVM6);
peakVM=[peakVM; maxVM6];

%% Region 7
j=1;
for i=1:length(Region7)
    index=find(Region7(i)==VM(:,1));
    if isempty(index)~=1
        VM7(j,:)=VM(index,:);
        j=j+1;
    end
end

for k=2:21
    aveVM7(k-1)=mean(VM7(:,k));
end
maxVM7=max(aveVM7);
peakVM=[peakVM; maxVM7];

%% Region 8
j=1;
for i=1:length(Region8)
    index=find(Region8(i)==VM(:,1));
    if isempty(index)~=1
        VM8(j,:)=VM(index,:);
        j=j+1;
    end
```

```
end

for k=2:21
    aveVM8(k-1)=mean(VM8(:,k));
end
maxVM8=max(aveVM8);
peakVM=[peakVM; maxVM8];

%% Region 9
j=1;
for i=1:length(Region9)
    index=find(Region9(i)==VM(:,1));
    if isempty(index)~=1
        VM9(j,:)=VM(index,:);
        j=j+1;
    end
end

for k=2:21
    aveVM9(k-1)=mean(VM9(:,k));
end
maxVM9=max(aveVM9);
peakVM=[peakVM; maxVM9];
```

APPENDIX B

REGIONAL PAMS AND RSS/TSS DATA

Occiput Convergence Study Data

Table 6: Occiput PAMS data by region.

Region	Coarsest 1.1 PAMS	Coarse 1.05 PAMS	Base 1.0 PAMS	Fine 0.95 PAMS
1	3302.993497	2562.714165	2510.171267	2725.44424
2	2458.628623	1947.570462	1829.600214	1998.869232
3	2923.592829	2646.215362	2271.564356	2430.449253
4	3980.007679	3154.305725	2945.245524	3092.397331
5	5004.402942	5175.911349	4458.537555	3997.681851
6	2888.38306	3071.067393	3016.605525	3295.100234
7	4743.66804	4137.993169	4114.022201	4487.377505
8	6671.394841	7076.488229	7107.880829	6687.642382
9	3707.468628	4106.87972	4113.445562	4205.20242

Table 7: Occiput RSS and TSS data by region.

Region	RSS	RSS	RSS	RSS	TSS
1	333563.145	26481.07735	46342.45293	0	869279.8978
2	211378.6973	2631.563836	28652.00045	0	2752038.187
3	243190.5869	46555.01379	25244.41042	0	1506380.16
4	787852.1291	3832.649208	21653.65452	0	319675.7109
5	1013487.355	1388224.75	212387.9799	0	115522.3581
6	165418.8598	50190.71377	77559.30315	0	131548.2545
7	65684.83829	122069.4144	139394.183	0	688205.3911
8	263.9825727	151201.0925	176600.3522	0	9179968.796
9	247738.9275	9667.353308	8419.320949	0	299653.7337
sum	3068578.521	1800853.628	736253.6575	0	15862272.49

Table 8: Occiput number of elements and RSS/TSS ratios by density.

Mesh Size (mm)	#Elements	RSS/TSS
1.1	88,127	0.193451381
1.05	98,089	0.11353062
1	111,803	0.046415396
0.95	125,118	0

Parietal Convergence Study Data

Table 9: Parietal PAMS data by region.

Region	Coarsest 1.1 PAMS	Base 1.0 PAMS	Fine 0.95 PAMS	Finest 0.90 PAMS
1	4637.355345	5125.15286	4132.074311	4142.985489
2	8022.368994	8320.113287	7481.669675	7925.523468
3	5661.135903	6016.657996	7040.510391	6439.1958
4	7263.346861	7368.709795	5792.690387	6043.690961
5	13008.24364	13019.05522	9675.607837	10379.00697
6	6647.298487	7109.836851	5775.698884	6299.005904
7	7353.866049	7531.815693	6662.378532	7015.982463
8	7539.080032	8444.265851	5686.204011	6182.257765
9	4610.81287	4436.217009	5311.219968	5328.660176

Table 10: Parietal RSS and TSS data by region.

Region	RSS	RSS	RSS	RSS	TSS
1	244401.5539	964652.7443	119.0538154	0	6233033.526
2	9379.055954	155701.1252	197006.1893	0	1653625.17
3	605377.2024	178538.1953	361579.2381	0	40157.79092
4	1487560.514	1755674.911	63001.28809	0	355095.5318
5	6912885.453	6969854.748	494770.3415	0	13983240.12
6	121307.7227	657446.8243	273850.2371	0	115997.4503
7	114165.3177	266083.9209	125035.74	0	141671.3702
8	1840966.666	5116680.582	246069.3266	0	209152.6716
9	515304.7551	796454.8077	304.1608711	0	1718536.71
sum	11851348.24	16861087.86	1761735.575	0	24450510.34

Table 11: Parietal number of elements and RSS/TSS ratios by density.

Mesh Size (mm)	#Elements	RSS/TSS
1.1	151,898	0.484707602
1	195,332	0.689600651
0.95	218,825	0.072053121
0.9	247,798	0

REFERENCES

Bloomfield, I.G., I.H. Johnston, and L.E. Bilston. "Effects of Proteins, Blood Cells and Clucose on the Viscosity of Cerebrospinal Fluid." *Pediatric Neurosurgery*, 1998: 246-251.

Boyd, Steven K., and Ralph Müller. "Smooth surface meshing for automated finite element model generation from 3D image data." *Journal of Biomechanics*, 2006: 1287-1295.

Centers for Disease Control and Prevention. *Injury Prevention & Control: Traumatic Brain Injury.* May 5, 2011. http://www.cdc.gov/traumaticbraininjury/statistics.html (accessed July 2011).

Chen, Ming, and David J Mogul. "A structurally detailed finite element human head model for simulation of transcranial magnetic stimulation." *Journal of Neuroscience Methods*, 2009: 111-120.

Cloots, R.J.H., H.M.T. Gervaise, J.A.W. Van Dommelen, and M.G.D. Geers. "Biomechanics of Traumatic Brain Injury: Influences of the Morphologic Heterogeneities of the Cerebral Cortex." *Annals of Biomedical Engineering*, 2008: 1203-1215.

Coats, B., and S.S. Margulies. "Material Properties of Human Infant Skull and Suture at High Rates." *Journal of Neurotrauma*, 2006: 1222-1232.

Coats, B., and S.S. Margulies. "Parametric Study of Head Impact in the Infant." *Stapp Carr Crash Journal*, 2007: 1-15.

Coats, Brittany. "Mechanics of Head Impacts in Infants." Philadelphia, PA: (Doctoral Dissertation) University of Pennsylvania, 2007.

Couper, Zac, and Faris Albermani. "Infant brain subjected to oscillatory loading: material differentiation, properties, and interface conditions." *Biomechanics and Modeling in Mechanobiology*, 2008: 105-125.

Dassault Systèmes. "Abaqus 6.10 Documentation." Vélizy-Villacoublay, April 2010.

DiMasi, Frank P, Rolf H Eppinger, and Faris A Bandak. "Computational Analysis of Head Impact Response Under Car Crash Loadings." *39th Stapp Car Crash Conference Procedings.* San Fransisco, CA: Society of Automotive Engineers, 1995. 425-438.

Galford, J., and J. McElhaney. "A Viscoelastic Study of Scalp, Brain, and Dura." *Journal of Biomechanics*, 1970: 211-221.

Khalil, Tawfik B, and Robert P Hubbard. "Parametric Study of Head Response by Finite Element Modeling." *Journal of Biomechanics*, 1977: 119-132.

Kim, Hyung Joo, and Colby C. Swan. "Voxel-based meshing and unit-cell analysis of textile composites." *International Journal for Numerical Methods in Engineering*, 2003: 977-1006.

McElhaney, J.H., J.L. Fogle, J.W. Melvin, R.R. Haynes, V.L. Roberts, and N.M. Alem. "Mechanical properties of cranial bone." *Journal of Biomechanics*, 1970: 495-511.

McPherson, G., and T. Kriewall. "The Elastic Modulus of Fetal Cranial Bone: A First Step Toward Understanding of the Biomechanics of Fetal Head Molding." *Journal of Biomechanics*, 1980: 9-16.

Mertz, Harold J. "A Procedure for Normalizing Impact Response Data." *SAE Technical Paper 840884.* SAE International, 1984.

Prange, M., and S.S. Margulies. "Regional, Directional, and Age-Dependent Properties of the Brain Undergoing Large Deformation." *Journal of Biomechanical Engineering*, 2002: 244-252.

Roth, Sébastien, Jean-Sébastien Raul, and Rémy Willinger. "Biofidelic child head FE model to simulate real world trauma." *Computer Methods and Programs in Biomedicine*, 2008: 262-274.

Ruan, J S, T Khalil, and A I King. "Dynamic response of the human head to impact by three-dimensional finite element analysis." *Journal of Biomechanical Engineering*, 1994: 44-50.

Takhounts, Erik G, et al. "Investigation of Traumatic Brain Injuries Using the Next Generation of Simulated Injury Monitor (SIMon) Finite Element Head Model." *Stapp Car Crash Journal*, 2008: 1-31.

Voo, L, S Kumaresan, F A Pintar, N Yoganandan, and A Sances. "Finite-element models of the human head." *Medical & Biological Engineering & Computing*, 1996: 375-381.

Watanabe, Dai, Kohei Yuge, Tetsuya Nishimoto, Shigeyuki Murakami, and Hiroyuki Takao. "Development of a Human Head FE Model and Impact Simulation on the Focal Brain Injury." *Journal of Computational Science and Technology*, 2008: 611-620.

Willinger, Remy, Ho-Sung Kang, and Baye Diaw. "Three-Dimensional Human Head Finite-Element Model Validation Against Two Experimental Impacts." *Annals of Biomedical Engineering*, 1999: 403-410.

Zar, Jerrold H. *Biostatistical Analysis.* Upper Saddle River, NJ: Pearson Prenctice Hall, 2010.